IOP Publishing

Analytical Evaluation of Uncertainty Propagation for Probabilistic Design Optimisation

Melanie Po-Leen Ooi, Arvind Rajan, Ye Chow Kuang and Serge Demidenko

Chapter 6

Real-world design optimisation problems: applications and usefulness

Moment-based uncertainty propagation methods sidestep the complications of finding the MPP that become apparent in the FORM. Furthermore, the moment approach provides optimiser stability (or convergence) compared to the MC method. Therefore, by utilising the analytical high-order moments accompanied by one of the parametric distribution fitting techniques, an arbitrary system response can be sustained through the use of robust design optimisation (RDO), reliability-based design optimisation (RBDO), or reliability-based robust design optimisation (RBRDO). Such an approach overcomes the limitations of the MPP methods as well as those of other moment-based approaches, thus providing more dependable results in probabilistic design optimisation.

This chapter applies the moment-based uncertainty evaluation method to several real-world examples to show its applicability in generating dependable and sturdy engineering systems.

6.1 The framework for probabilistic design optimisation

Figure 6.1 presents the unified moment-based probabilistic optimisation framework, which will be referred to as the *polynomial moment* (PolyMoment) -based approach in the following discussions. This framework is generic and can be simplified depending on the optimisation paradigm employed, i.e. RDO, RBDO, or RBRDO. The steps used to apply the PolyMoment approach are elaborated in this section, which makes reference to the previous chapters of this book. The remainder of this chapter presents real-world applications of PolyMoment.

As shown in the flowchart, once the probabilistic optimisation problem has been formulated by identifying the objective, performance, and constraint functions according to (3.2), (3.9), or (3.20), the following five steps are executed:

doi:10.1088/978-0-7503-4931-4ch6

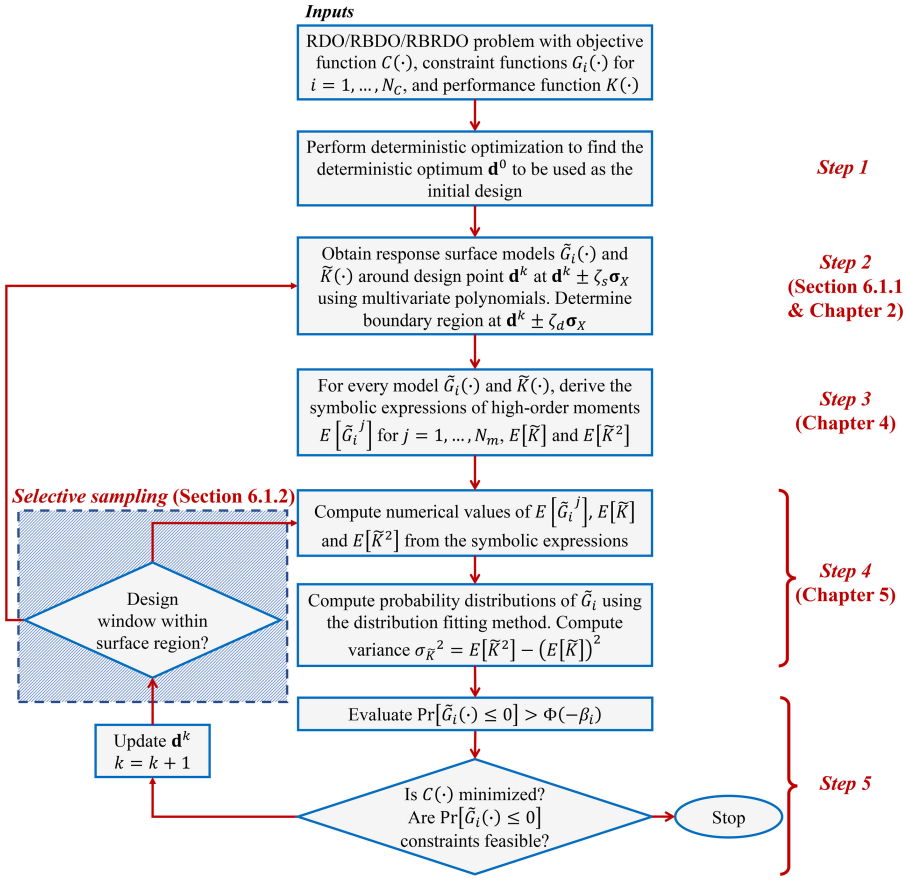

Figure 6.1. The framework of the polynomial moment (PolyMoment)-based probabilistic optimisation for RDO, RBDO, and RBRDO.

Step 1: Find the deterministic optimum design using the formulation shown in (3.1) and use it as the initial design $\mathbf{d}^{k=0}$ of the moment-based probabilistic optimisation; $\mathbf{d}^k$ denotes the design point at the kth iteration.

Step 2: Model the response surface of the constraint function $G_i(\cdot)$ for $i = 1,\ldots,N_c$ (for RBDO/RBRDO) and the performance function $K(\cdot)$ (for RDO/RBRDO) using a polynomial (refer section 6.1) around design point $\mathbf{d}^k$ using the surface region constant ζ_s and the vector of standard deviation of the random variables $\boldsymbol{\sigma}_X$; then determine the *design window* for *selective sampling* using the design window constant ζ_d and $\boldsymbol{\sigma}_X$ (refer to section 6.1.2).

Step 3: For RBDO and RBRDO, find the closed-form expressions of the high-order moments $E\left[\widetilde{G}_i^{\,j}\right]$ for $i = 1,\ldots,N_c$ and $j = 1,\ldots,N_m$ using the analytical moment propagation framework introduced in chapter 4. For RDO and RBRDO, find $E[\widetilde{K}]$ and $E[\widetilde{K}^2]$. Here, $\widetilde{G}_i(\cdot)$ and $\widetilde{K}(\cdot)$ denote the approximated $G_i(\cdot)$ and $K(\cdot)$, respectively. Evaluate the numerical values of the moments.

Step 4: For RBDO and RBRDO, find the probability distribution of the performance functions using one of the moment-based distribution fitting methods studied in chapter 5. For RDO and RBRDO, compute the variance of $\widetilde{K}$ using $\sigma_{\widetilde{K}}{}^2 = E[\widetilde{K}^2] - (E[\widetilde{K}])^2$.

Step 5: Finally, ensure that the constraints $\Pr[G_i(\mathbf{d}, \mathbf{X}) \leqslant 0] > \Phi(\beta_i)$ are met using the estimated probability distribution (for RBDO and RBRDO) and that the objective function $C(\cdot)$ has been minimised. If either of the conditions is not met, update design point $\mathbf{d}^k$ for $k = k + 1$ using the chosen optimiser and go to step 2 if the design window exceeds the response region; or step 3 otherwise (refer to section 6.1.2).

6.1.1 Local response surface modelling using multivariate polynomials

In problems whose large-scale optimisation would involve the use of costly simulations, metamodels (or surrogate models) are used instead of actual simulations to assess the performance and constraints [1]. Polynomial metamodels are a popular choice for this purpose [2, 3]. Studies [2, 4] have shown that the use of polynomial metamodels can significantly reduce the cost of probabilistic optimisation, even when functional relationships between performance functions and input variables are available. Section 3.2.3 covers techniques commonly used to express system responses using multivariate polynomials. The choice of model for the PolyMoment framework given in figure 6.1 is up to the user.

Although polynomial metamodels can greatly improve computational efficiency, using them as a global approximation sacrifices accuracy when the constraint and performance functions are highly nonlinear. Therefore, local approximations of the responses can be made at every iteration. Local approximations using second-order polynomials are some of the most commonly used approaches, even in MPP-based optimisation methods [2, 4]. The results of these studies have demonstrated that this strategy significantly improves both the computational efficiency and the accuracy of the RBDO computation. The next subsection presents a selective sampling technique introduced in [2] for the surface reconstruction procedure, which is a way of further boosting the computational efficiency.

6.1.2 The selective sampling technique

Selective sampling, as proposed by [2], balances global and local modelling by determining the need for a new local response surface based on a mechanism that uses a *surface region* and a *design window* (explained below). This approach improves computational efficiency by only constructing a new local response surface when deemed necessary.

As shown in figure 6.1, the PolyMoment-based optimisation starts by finding the deterministic optimum $\mathbf{d}^{k=0}$; then, the response surface is locally approximated around the intervals:

$$\mathbf{d}^k \pm \zeta_s \boldsymbol{\sigma}_X. \tag{6.1}$$

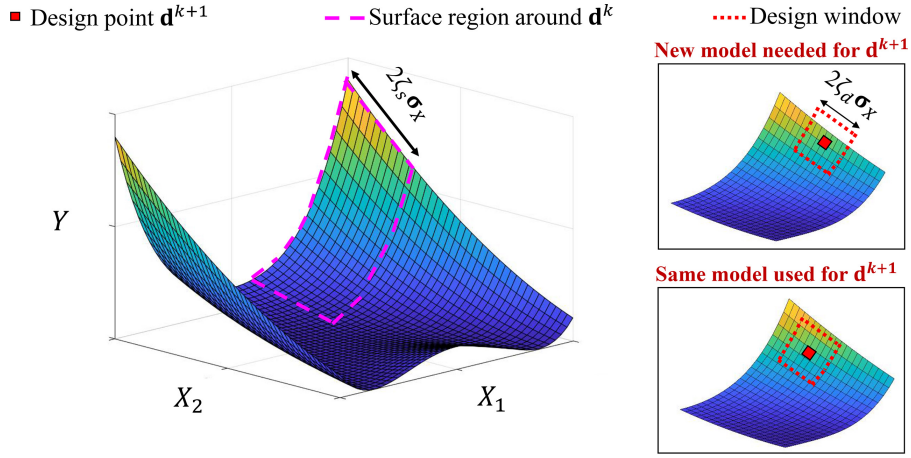

Figure 6.2. An illustration of the selective sampling technique using the highly nonlinear Rosenbrock function [6]. The figure shows the situation in which a new model is required when the design point's design window exceeds the surface region and vice versa.

The value of the surface region constant ζ_s is typically selected based on a multiplicative factor of 1.2–1.5 times the target reliability index β used in the optimisation problem.

For example, 1.2β is used for moderately nonlinear problems and 1.5β is used for highly nonlinear ones [5]. The design window constant ζ_d is a smaller value ($\zeta_d < \zeta_s$) used for the selective sampling technique. The mechanism of the technique is illustrated in figure 6.2 using the highly nonlinear Rosenbrock function [6].

Consider the case in which a local response surface (depicted by dashed lines) is constructed around $\mathbf{d}^k$ using the intervals (6.1). In the next iteration, the design point $\mathbf{d}^{k+1}$ is changed and a decision about the need for a new model is made using the design window, which is defined as $\mathbf{d}^{k+1} \pm \zeta_d \boldsymbol{\sigma}_X$ (depicted by dotted lines). As shown in figure 6.2, when the design window around $\mathbf{d}^{k+1}$ exceeds the boundaries of the existing surface region, a new local response surface is constructed around $\mathbf{d}^{k+1}$. On the other hand, if the design window remains within the existing surface region, the current model is used. As a result of implementing the selective sampling technique, the local response surface does not have to be created at every iteration, thus improving the overall efficiency of the probabilistic optimisation process.

6.2 Lithium-ion batteries: a reliability-based design optimisation framework

In complex engineering systems, the relationship between the output of interest and the input variables is not always clear, so numerical algorithms such as the finite element method are used to calculate the output variables. The input–output relationship in an FE model can only be approximately calculated using basic mathematical models, which are then locally evaluated for further examination including uncertainty evaluation. A prime example is the modelling of the

mechanical strength of lithium-ion batteries when they are subjected to sudden impact [7]. The goal is to understand the relationship between the mechanical strength of the battery and three inputs: displacement, surrounding temperature, and strain rate. The model should consider uncontrolled factors, such as manufacturing tolerances, shocks, and vibrations, which affect the battery strength estimation. The purpose of the model is to study the behaviour of the battery's mechanical strength and determine optimal input values that result in the minimum or maximum mechanical force.

Modelling the mechanical strength of a *lithium-ion battery* (LIB) when it is subjected to sudden impact is a complex task due to various variables such as stochastic and dynamic loads, variations in material properties, and interactions among elements. The force developed in an LIB during a crash is an important factor in determining its resistance to tensile impact and serves as a basis for its new mechanical design.

To obtain accurate results, the uncertainties of the inputs and their impact on the mechanical strength must be considered using an uncertainty evaluation toolbox, as discussed in previous chapters of the book. An FE model is used as an initial step to analyse the mechanical forces experienced by the battery in relation to its inputs through the use of surface plots or optimisation algorithms. However, there are two challenges associated with this method. First, repeating the FE model's execution for uncertainty analysis in the generation of surface plots or optimisation significantly increases the computational load. Second, the output mechanical force calculated using the FE model does not account for the uncertainties of the inputs.

A Monte Carlo simulation was considered but discarded, even though it is the most robust and effective method for this type of uncertainty evaluation. MC simulation involves the generation of multiple independent realisations of input quantities using known probability distributions, which are then used to calculate the output probability distribution. The mean and standard deviation of the output can also be obtained. However, the computational time required to run the MC simulation can be prohibitively long if the FE model takes 10 min per execution and 104 realisations are required to obtain a single distribution.

Instead, this case study employs an *artificial neural network* (ANN) to obtain a global model of the battery's mechanical strength and applies the PolyMoment-based approach (see figure 6.3) to reduce the computational load. This approach considers variations in the inputs and provide high-order statistics such as the mean, standard deviation, skewness, and kurtosis, as well as the probability distribution of the mechanical force.

6.2.1 The finite element model of the lithium-ion battery

The ABAQUS/Explicit version 6.14 software [8] is used to model the mechanics of the lithium-ion battery with fully coupled thermal stress analysis to understand the interaction effects of various factors on the maximum crushing load of the battery pack. The model, described in [7], includes components such as the battery casing,

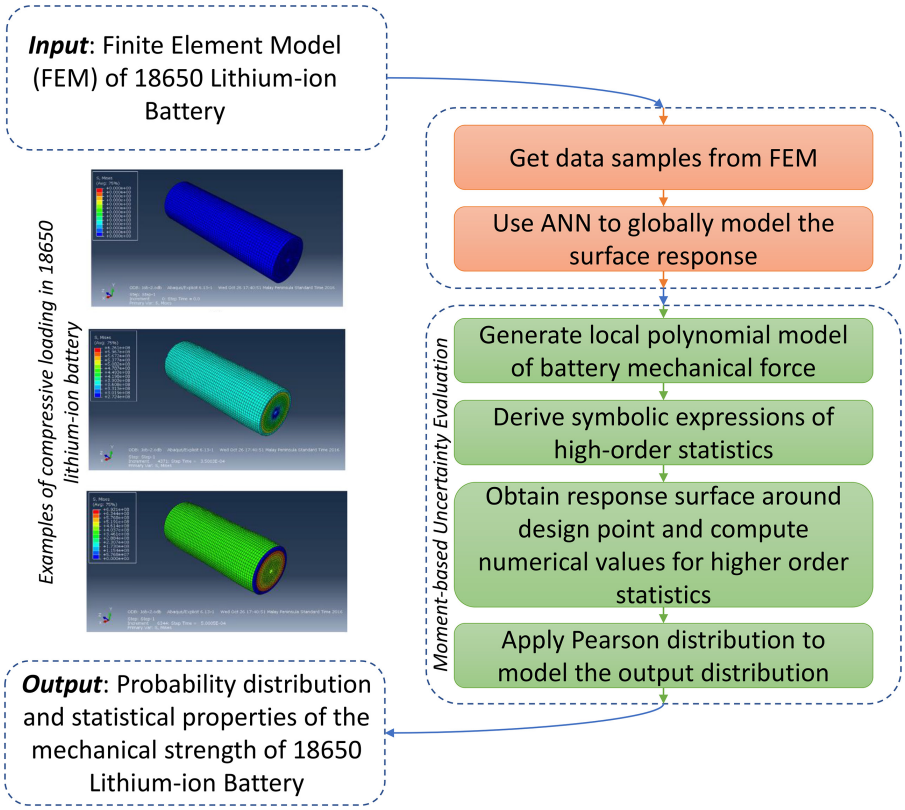

Figure 6.3. A framework for RBDO that utilises moment-based uncertainty evaluation with an FE Model of the 18650 LIB to obtain the probability distribution and statistical properties of its mechanical strength.

jelly roll, composites, and isolators. Smaller components are ignored, as their deformation is largely insignificant according to [9].

It should be noted that studies such as [10–12] have developed constitutive mechanical models for the failure assessment of battery packs. In this study, the battery casing, which is made of steel, and the jelly roll, modelled as crushable foam, undergo significant plastic deformation during mechanical loading and are considered in the analysis. This study uses a homogenised mechanical model of the jelly roll from [10] to reduce computational time, while still accurately replicating the load and displacement of the 18650 LIB. This allows for finer meshing and more accurate deformation and failure mechanism predictions in response to the applied load.

The FE model was validated by comparing simulation results with experimental data, which showed good agreement. The force–displacement plot, force–temperature plot, and force–strain rate plot were compared for the results of the simulation and the experiment; the comparison revealed similar levels of accuracy. The FE model was used to obtain compressive force data for variations in displacement, strain rate, and temperature. The FE model snapshots (see examples on the left-hand side of figure 6.3) showed the effect of compression loading on the battery structure.

6.2.2 Incorporating moment-based uncertainty evaluation

In this study, data samples were collected from the finite element model using *Latin hypercube sampling* [13] and an ANN was trained using 70% of the collected data to build a global model of the mechanical force in a lithium-ion battery, as shown in [7]. The temperature values ranged from 10 °C to 50 °C with an interval of 10 °C, the displacement ranged from 2mm to 8mm with an interval of 2mm, and the strain rate ranged from 0.05 to 0.20 mm s^{-1} with an interval of 0.05 mm s^{-1}. The ANN model showed high prediction accuracy with a coefficient of determination (R^2) of 0.999 74 (figure 6.4).

To consider the uncertainties in the inputs and obtain the statistical properties and probability distribution of the mechanical force, the model-based uncertainty evaluation described in section 4.2 was performed on the ANN model. This evaluation required the use of a multivariate polynomial to represent the relationship between the inputs and the outputs, and therefore a local model of the mechanical force F_l was established using a general three-variable second-order polynomial equation:

$$F_l(\boldsymbol{X}) = a_{00} + \sum_{i=1}^{N} a_{0i} X_i + \sum_{i=1}^{N} a_{ii} X_i^2 + \sum_{i=1}^{N} \sum_{j=i+1}^{N} a_{ij} X_i X_j + \epsilon, \tag{6.2}$$

where $\boldsymbol{X} = \{X_1,\ldots,X_N\}$ denotes the input variables, $N = 3$ is the number of variables, $\{a_{00}, a_{0i}, a_{ii}, a_{ij}\}$ is the set of model coefficients, and ϵ is the modelling (or approximation) error.

The symbolic expressions for the higher-order statistics of the mechanical force were then computed using a toolbox described in section 4.2. It is important to note that only the finite element runs used to train the ANN model were needed to compute the probability distribution of the mechanical force. No additional finite element simulations were required, as the changes in the response surface model

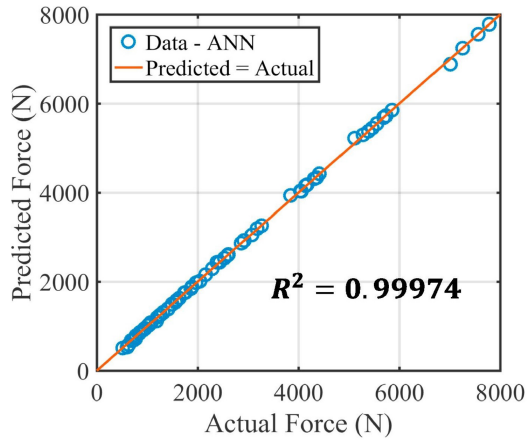

Figure 6.4. A comparison between the mechanical force predicted by the ANN model and the actual experimental data obtained from the finite element (FE) model. Reprinted from [7], Copyright 2018, with permission from Elsevier.

were captured in the coefficients. However, the form of the model remained unchanged.

Next, the coefficients of the polynomial model were obtained using the Box–Behnken design approach for the design of experiments and the least-squares method [14]. The data samples were collected for the design of experiments to obtain the numerical values of the higher-order statistics. The local model was constructed within a range of $\pm 3\sigma X$, where σX is the standard deviation vector of the input variables.

The least-squares method was employed to build the model, making it possible to assume that the error term ϵ followed a normal distribution with zero mean and standard deviation $\sigma\epsilon$ [14]. This additional random variable was incorporated when using the toolbox from section 4.2 to compute the higher-order statistics, considering the modelling error of F_l when calculating its uncertainty. The calculated higher-order statistics were then used with the Pearson system (described in section 2.5.5) to approximate the distribution of the mechanical force.

6.2.3 The resultant design

The probability distributions obtained through the PolyMoment-based RBDO method are compared to those obtained through Monte Carlo simulation using finite element simulation data in figure 6.5. The comparison is made for a displacement of 5mm, a temperature of 30 °C, a strain rate of 0.125 mm s^{-1}, and with coefficients of variation of 0.01 and 0.05. The histogram of the Monte Carlo

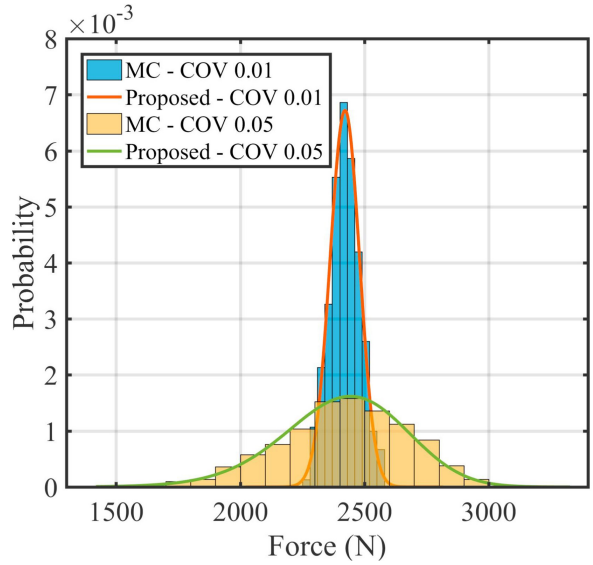

Figure 6.5. A comparison of the probability distributions produced by PolyMoment-based RBDO and a Monte Carlo simulation using the FE data for a displacement of 5mm, a temperature of 30 °C, and a strain rate of 0.125 mm s^{-1} with coefficients of variance (COVs) of 0.01 and 0.05. Reprinted from [7], Copyright 2018, with permission from Elsevier.

simulation was generated with a sample size of 500. The results in figure 6.5 demonstrate that the distributions obtained from the proposed framework are in good agreement with the Monte Carlo simulation. In addition, the figure shows that as the coefficient of variation of the inputs increases, the spread of the mechanical strength distribution also increases. Although the study assumes normal distributions for the inputs, the proposed method is capable of handling non-normal distributions as well.

PolyMoment is capable of performing probabilistic analyses under various uncertainty conditions, including different distributions and input uncertainties, without requiring additional ANN model building or FE simulation evaluations. This capability is of significant value, especially when FE models require high computational times for each execution or when design optimisation algorithms necessitate repeated evaluations of output probability distributions or sensitivities.

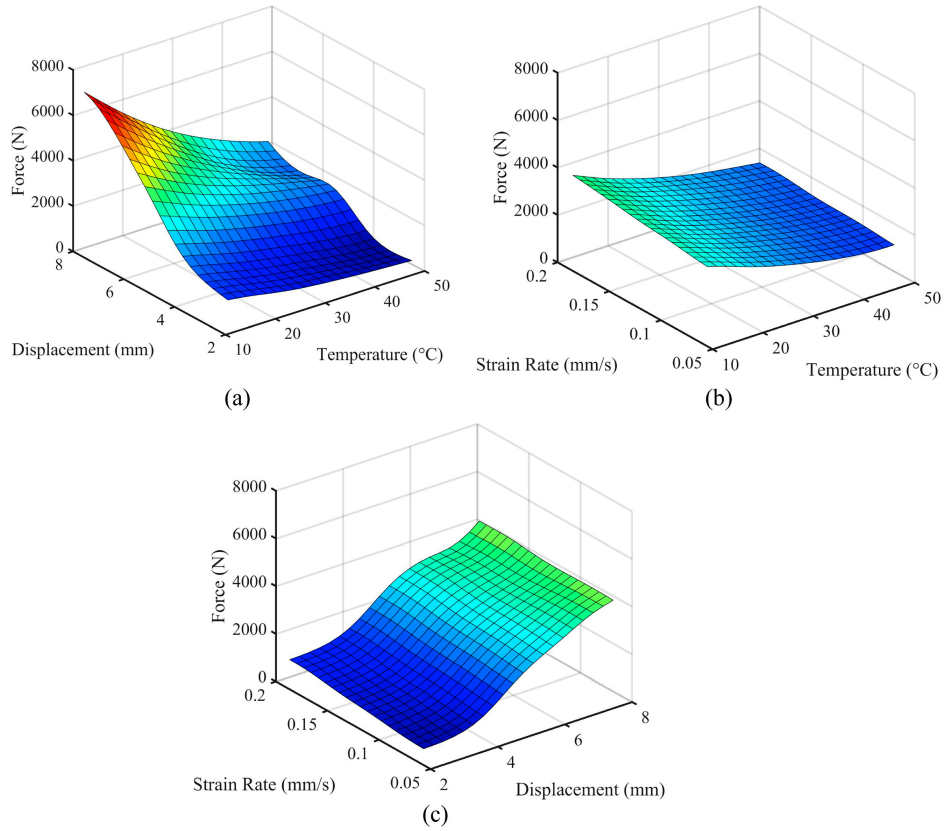

Figure 6.6. A depiction of the relationship between the input variables and the mean mechanical strength of an LIB; one input is held constant in each plot. (a) A constant strain rate of 0.19 mm s^{-1}, (b) a constant displacement of 7.66 mm, and (c) a constant temperature of 10.47 °C. The input variables are assumed to follow a normal distribution with a coefficient of variation of 0.01. Reprinted from [7], Copyright 2018, with permission from Elsevier.

The mean mechanical force computed by the PolyMoment framework was used to generate the three surface plots in figure 6.6, which illustrate the influence of inputs on the mechanical force experienced by the battery. By keeping one of the inputs constant, it is possible to observe the trend in figure 6.6. This trend remains consistent regardless of the constant values used, allowing one to infer the sensitivity of the force experienced by the battery force with respect to its inputs.

The surface plots in figure 6.6 demonstrate that the mechanical strength of the battery increases with increasing strain rate and displacement, but decreases with increasing temperature. These results are aligned with experimental results, which show that larger external impacts result in higher mechanical stresses and strains. Higher temperatures decrease battery strength due to decreased hardness and toughness. The sequential quadratic programming algorithm [15] and other advanced optimisation methods (genetic algorithm [16], stepwise optimisation [17, 18]) show that the maximum mean mechanical strength (7530 N) can be achieved at displacement of 8 mm, a temperature of 10 °C, and a strain rate of 0.2 mm s^{-1}.

From the plots, it can be concluded that: (1) the proposed probabilistic framework accurately predicts the probability distribution of the LIB's mechanical strength; (2) lower displacement and temperature result in higher battery strength; (3) displacement and temperature have equal impacts on battery strength, while the strain rate has a lower impact.

The application of the PolyMoment framework offers a probabilistic method for battery design that takes account of uncertainties both inside and outside the battery, which is vital for battery dependability and security. These findings are especially relevant to battery manufacturers who aim to meet safety regulations and prevent accidents in electric vehicles.

6.3 Vehicle design based on side-impact crashworthiness: the application of a reliability-based robust design optimisation problem

This section examines a vehicle side-impact crashworthiness study [19], which is an optimisation problem with nine design variables, eleven random variables, and ten constraint functions and is commonly used as a benchmark for new probabilistic optimisation methods. The aim is to reduce the weight of the vehicle $W(\mathbf{X})$ and the variance of the performance function $K(\mathbf{X})$ while improving side-impact crash protection for passenger safety. To achieve this, the European Enhanced Vehicle-Safety Committee side-impact procedure [20] is utilised to establish the reliability constraints of the performance functions.

6.3.1 Problem formulation

The problem formulation (from [19]) is:

$$
\begin{aligned}
&\text{minimize: } C = (\mathbf{X}) = w_1 \frac{W}{W_0} + w_1 \frac{\sigma_K^2}{\sigma_0^2}, \\
&\text{subject to: abdomenload} < 1\text{kN}, \\
&\qquad \text{upper/middle/lower viscous criteria} < 0.32\ \text{ms}^{-1}, \\
&\qquad \text{upper/middle/lower rib deflection} < 32\ \text{mm}, \\
&\qquad \text{pubicsymphysisforce} < 4\text{kN}, \\
&\qquad \text{velocity of B-pillar at middle point} < 9.9\ \text{mm ms}^{-1}, \\
&\qquad \text{velocity of front door at B-pillar} < 15.7\ \text{mm ms}^{-1}, \\
&\text{where:} \quad \mathbf{d}^L \leqslant \mathbf{d} \leqslant \mathbf{d}^U, \quad \text{and} \quad \beta = 1.282,
\end{aligned}
\tag{6.3}
$$

where $w_1 = 0.5$ and $w_2 = 0.5$ are the weights, $W_0 = 29.05$ kN is the initial weight, and $K_0 = 1.4781$ mm is the initial variance of the performance function based on the original design points given in [19]. The constraint and performance functions, initial design points, statistical information, and details of the random variables are given in [19]. The target reliability index for all constraint functions is $\beta = 1.282$.

6.3.2 Resultant design

The performance function that represents the safety component of the design objective in this RBRDO problem is the lower rib deflection. To assess its robustness and reliability, we adopt a combination of moment-based robustness analysis using univariate DRM and PMI (from section 3.1) and reliability analysis using PMA (from section 3.2). The results are compared with those obtained from the PolyMoment-based RBRDO method, as depicted in figure 6.1, which provides a comprehensive framework for performing both probabilistic analyses. The final design outputs are tabulated in table 6.1.

In addition to the total number of function evaluations and the accuracy of meeting the probability constraints, the accuracy with which σ_K is computed is also considered as a performance metric. Unlike the previous examples, the actual reliabilities computed by the MC method are presented in a radar chart in figure 6.7. Since the failure probability is 10% ($\beta = 1.282$), the ideal solution is a radar line that stays within the two outermost polygon regions. Any radar line that crosses the

Table 6.1. The performance of the robustness analysis of the PMI, DRM, and proposed PolyMoment methods in vehicle side-impact crashworthiness evaluation. FEV denotes the function evaluation counts [21].

	Optimum design			
Method	W (kN)	Calculated σ_K (mm^2)	Actual σ_K (mm^2)	Total FEV counts
PMI and PMA	28.7780	0.0618	0.6254	4590
DRM and PMA	25.8685	0.4144	0.4645	4940
PolyMoment	27.6034	0.1633	0.1635	1526

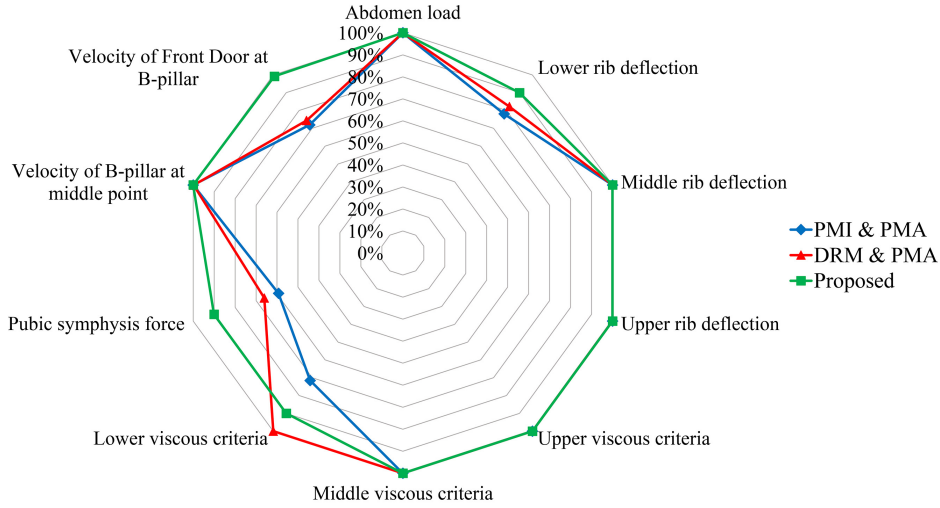

Figure 6.7. The probability of satisfying the constraint functions for the vehicle side-impact crashworthiness problem. Reproduced from [21], CC BY 3.0.

second outermost boundary towards the centre indicates a design violation for that specific reliability constraint.

Table 6.1 compares the results of three RBRDO techniques in terms of side-impact crashworthiness. All three methods offer a significant reduction in vehicle weight and lower rib cage deflection variance. However, the PolyMoment method outperforms the others by yielding optimal results three times faster.

The PolyMoment method also produces a design that offers a good balance of vehicle weight and safety, while the variance estimations produced by the MC method reveal that the DRM and PMI methods underestimate the variance. This results in lighter but less safe designs. For example, if the DRM is used, the variance is underestimated at 0.4144 mm^2, which might be overlooked by the designer, as the true value is 0.4645 mm^2. Increasing the quadrature points or using bivariate DRM could improve accuracy, but at the cost of increased function evaluations. The PMI method has an even greater variance underestimation.

Although the PMA with DRM appears to be the best option for weight optimisation based on table 6.1, the radar chart in figure 6.7 indicates that this design is unreliable and fails to meet safety standards when validated using the MC method. This aligns with the literature [22], which states that multiple MPP iterations can lead to unreliable designs. However, the design solution produced by the PolyMoment method always satisfies the failure probability constraint of less than 10%.

6.4 Fuel cells: parameter optimisation for reliable and robust operation

Hydrogen fuel cells are seen as a promising energy storage technology due to their environmental friendliness and efficiency compared to traditional combustion

technologies. The polymer electrolyte membrane (PEM) fuel cell is considered one of the most promising types due to its high power output, low operating temperature, efficiency, high current density, and structural safety [23–26]. These benefits make PEM fuel cells suitable for small-scale power generation and for use in the automobile industry.

The operation of a PEM fuel cell is shown in figure 6.8. It consists of an electrolyte sandwiched between two electrodes (the anode and cathode), with bipolar plates on both sides that distribute hydrogen and oxygen gases and serve as current collectors. Hydrogen gas flows to the anode, where it is separated into protons and electrons by a catalyst; the protons flow through the membrane to the cathode and the electrons flow through an external circuit to generate electricity. On the cathode side, oxygen reacts with the hydrogen ions to form water, and the exothermic reaction generates heat [27].

Research has been conducted on PEM fuel cells to optimise their efficiency. The first fuel cell models date back to the early 1990s [27]. More comprehensive models were later developed, including a dynamic model that incorporated six submodels [29]. Other studies optimised operational parameters using novel algorithms [30, 31], a battery–capacitor hybrid system [32], and stochastic dynamic programming [33]. However, no study has considered the uncertainties in the operating parameters and their propagation to output uncertainties in PEM fuel cell optimisation.

This subsection utilises a PolyMoment framework that incorporates uncertainty evaluation into the design optimisation loop of a PEM fuel cell. This approach will result in a more robust and cost-efficient PEM fuel cell, taking into account factors

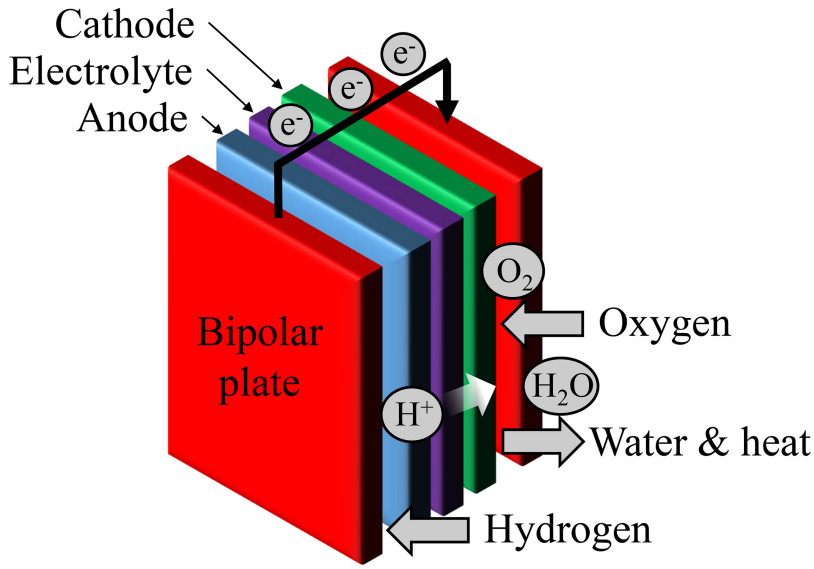

Figure 6.8. The polymer electrolyte membrane (PEM) fuel cell. Reprinted from [28], Copyright 2018, with permission from Elsevier.

such as manufacturing variations, material variations, and uncontrollable operating environments [34–38].

6.4.1 Problem formulation

The problem statement focuses on optimising the output power of a PEM fuel cell described in [29] while considering the hydrogen mass flow rate (equation (6.4)) in an economical design. The study uses a dynamic fuel cell model made up of six components and considers the hydrogen mass flow rate to be an important parameter. The output power of the fuel cell is dependent on five inputs, and the study aims to analyse the uncertainty of the outputs (fuel cell power and hydrogen flow rate) and perform a sensitivity analysis to identify the optimal parameters for a reliable and robust design. The PolyMoment framework is proposed to perform the analysis in an accurate and efficient manner.

$$W_{\mathrm{H}_2} = \frac{I_{\mathrm{st}}}{2F} M_{\mathrm{H}_2} n \lambda_{\mathrm{an}}, \tag{6.4}$$

where I_{st} is the stack current, F is the Faraday constant, M_{H_2} is the molecular mass of hydrogen, n is the number of cells, and λ_{an} is the hydrogen excess rate.

The efficiency of the fuel cell's output power is influenced by various parameters, such as the stack current I_{st}, the stack temperature T, the oxygen excess ratio λ_{ca}, the hydrogen excess ratio λ_{an},, and the inlet air humidity $\varphi_{\mathrm{ca,\ in}}$ (refer to figure 6.9). These operating conditions are usually optimised for maximum output power efficiency and minimum hydrogen consumption. To assist this optimisation process, response surface methodology (RSM) is used to describe the relationship between the output and the inputs of the system. This study takes account of the uncertainties in fuel cell output power and hydrogen consumption in the optimisation process, as illustrated in figure 6.10.

The response surface of the PEM fuel cell's output power is constructed using a second-order polynomial model:

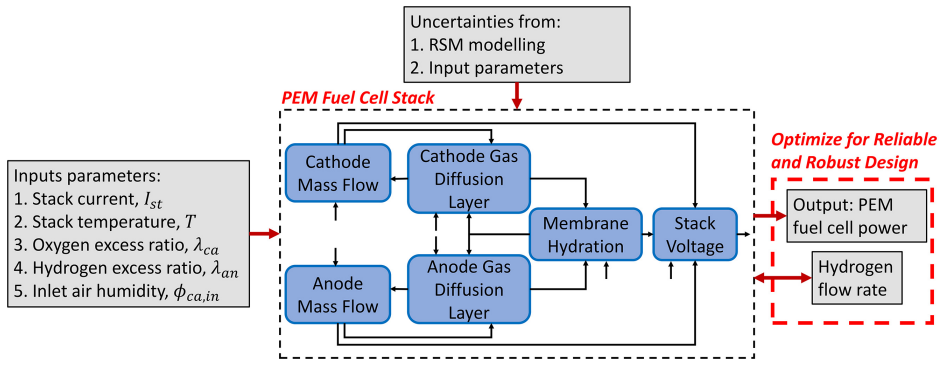

Figure 6.9. The relationships and modelling of variables in the optimisation of PEM fuel cell design with a focus on optimising power subject to a low hydrogen mass flow rate. Reprinted from [28], Copyright 2018, with permission from Elsevier.

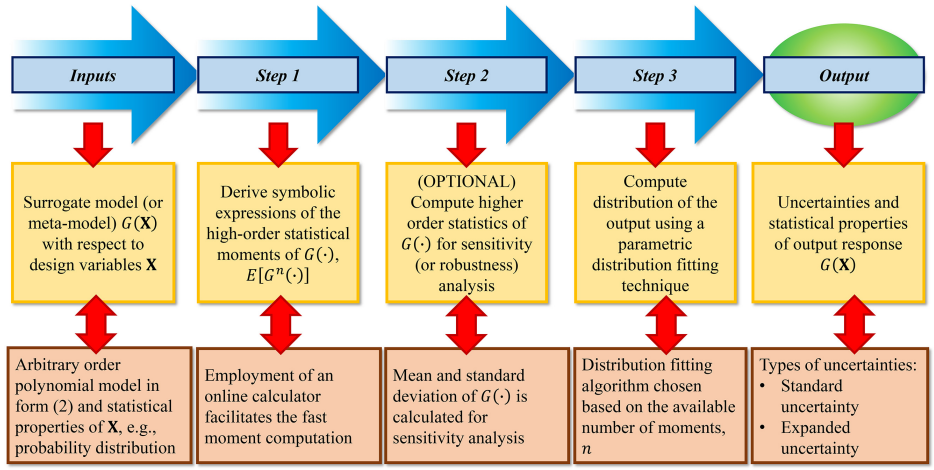

Figure 6.10. The framework used to apply PolyMoment to determine the statistical properties of the PEM fuel cell. Reprinted from [28], Copyright 2018, with permission from Elsevier.

Table 6.2. The minimum and maximum values of the design variables used to construct the RSM model of PEM fuel cell output power and the statistical properties (probability distribution and coefficient of variation) attributed to the respective design variables for probabilistic analysis.

Design variable	Minimum value	Median value	Maximum value	Probability distribution	Coefficient of variation
Stack current, I_{st} (A)	36.0	43.0	50.0	Uniform	0.01
Stack temperature, T (°C)	55.0	60.0	65.0	Uniform	0.01
Oxygen excess ratio, λ_{ca}	1.5	2.5	3.5	Normal	0.01
Hydrogen excess ratio, λ_{an}	1.1	1.3	1.5	Normal	0.01
Inlet air humidity, $\phi_{ca,\,in}$	0.6	0.8	1.0	Uniform	0.01

$$G(\mathbf{X}) = a_{00} + \sum_{i=1}^{N} a_{0i} X_i + \sum_{i=1}^{N} a_{ii} X_i^2 + \sum_{i=1}^{N-1} \sum_{j=i+1}^{N} a_{ij} X_i X_j + \varepsilon. \tag{6.5}$$

Here, $G(\cdot)$ denotes the output response, $\mathbf{X}$ denotes the vector of design variables, N denotes the number of design variables, and $\{a_{00},\ a_{0i},\ a_{ii},\ a_{ij}\}$ is the set of model coefficients. Table 6.2 presents the lower and upper bounds of the input stack current, stack temperature, oxygen excess ratio, hydrogen excess ratio, and inlet air humidity.

The first step is to derive symbolic expressions for the high-order moment of $G(\cdot)$ using the toolbox in section 4.2. The next step involves substituting the numerical

values of the model coefficients and the other parameters of X to obtain the statistical parameters of $G(\cdot)$. The optional third step is a sensitivity or robustness analysis.

6.4.2 Sensitivity analysis

This study aims to find the optimal combination of design variables that results in the highest output power P and the lowest hydrogen mass flow rate W_{H_2} for a PEM fuel cell. To ensure economical operation, it is crucial to minimise W_{H_2}. To determine the design's robustness, the sensitivities of the mean and standard deviation of P and W_{H_2} with respect to the stack current I_{st} and the hydrogen excess ratio λ_{an} are analysed using the 3D surface plot shown in figure 6.11.

The other parameters were kept constant and were assumed to have a coefficient of variation of 0.01. As can be seen in figures 6.11(a) and (b), the mean and standard deviation of the output power are more sensitive to changes in I_{st} than to changes in λ_{an}. However, both I_{st} and λ_{an} have an equal impact on the mean and standard deviation of W_{H_2}, as shown in figures 6.11(c) and (d).

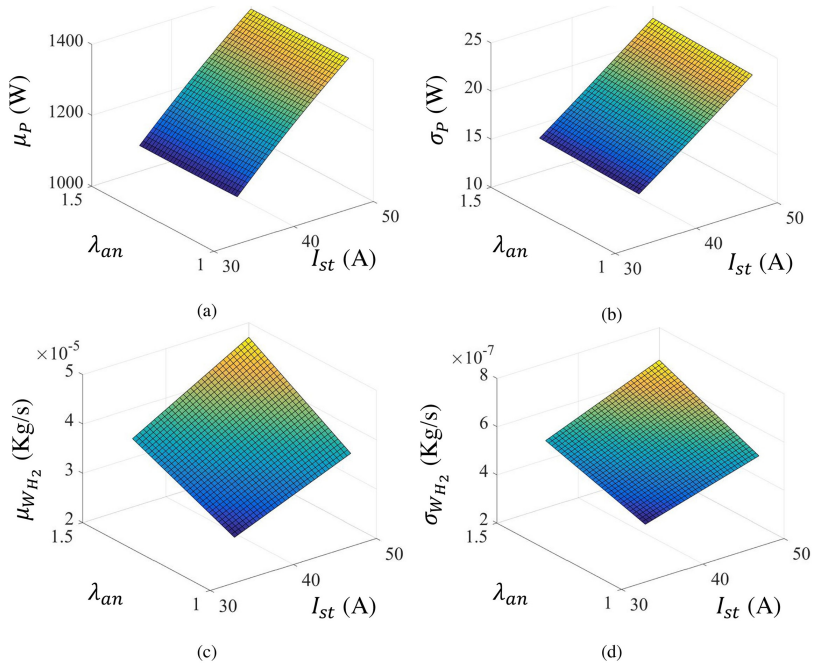

Figure 6.11. Surface plots showing the influence of the stack current I_{st} and hydrogen excess ratio λ_{an} on the (a) mean and (b) standard deviation of the output power P as well as (c) on the mean and (d) standard deviation of the hydrogen mass flow rate. The other parameters are kept constant, as follows: the stack temperature is 60 °C, the oxygen excess ratio is 2.5, and the air humidity ratio is 0.8. All the parameters are assumed to have distinct probability distributions with a coefficient of variation of 0.01. Reprinted from [28], Copyright 2018, with permission from Elsevier.

6.4.3 Determination of the optimal operating conditions for RBDO and RBRDO

There are two ways to optimise the design of a PEM fuel cell for optimal power output while maintaining a low hydrogen flow rate of 3e−5 kg s^{-1}: (1) reliability-based optimisation with a 99% confidence constraint and (2) reliability-based robust optimisation, which also minimises the standard deviation of the output power and the hydrogen flow rate.

The objectives and constraints are set using a sequential quadratic programming algorithm [39], and the PolyMoment framework is used to calculate the reliability and the standard deviation. The Pearson system of distributions is used for approximation. The output power is represented by equation (6.5) with $N = 5$, and the hydrogen mass flow rate is given by equation (6.4).

For this case study, the problem of reliability-based optimisation can be mathematically formulated as:

$$\begin{aligned} &\text{Maximise: } \mu_{G(\mathbf{d},\,\mathbf{X})}, \\ &\text{subject to: } W_{H_2}(\mathbf{d}, \mathbf{X}) \leqslant 3e^{-5} \text{ kg}, \\ &\quad \text{where: } \mathbf{d}^{L} \leqslant \mathbf{d} \leqslant \mathbf{d}^{U} \text{ and } \mathbf{d} = E[\mathbf{X}], \end{aligned} \tag{6.6}$$

where $\mathbf{d}^{L}$ and $\mathbf{d}^{U}$ are the lower and upper bounds of the vector of design variables $\mathbf{d}$, respectively.

Based on the optimisation results, the highest mean output power of 1329.56 W can be achieved with the following parameters: a stack current of 42.16 A, a stack temperature of 63.98 °C, an oxygen excess ratio of 3.50, a hydrogen excess ratio of 1.10, and an inlet relative air humidity of 0.63. These values also ensure, with 99% confidence, that the hydrogen flow rate stays below 3e−5 kg s^{-1}. The results are even consistent with those of other advanced optimisation algorithms, such as the genetic algorithm [16] and stepwise optimisation [17, 18].

Figure 6.12 compares the results of the PolyMoment framework with Monte Carlo simulations that include and exclude uncertainties in the hydrogen mass flow rate. The Monte Carlo simulations, which are considered to represent the current state of the art in the field but are computationally intensive, demonstrate close agreement with the results from PolyMoment. Furthermore, PolyMoment offers a more computationally efficient approach than the Monte Carlo simulations.

However, the Monte Carlo simulation that excludes uncertainties in the hydrogen mass flow rate has a 50% chance of exceeding the design constraint for the hydrogen mass flow rate, which could lead to increased hydrogen consumption and cost. This highlights the importance of considering uncertainties when optimising for the power output in this field. The maximum power output that can be attained without considering uncertainties is 1545.25 W, as reported in [29].

The standard deviations of the output power and the hydrogen flow rate of the PEM fuel cell can be reduced to improve the quality of the design. This results in a robust design that is less affected by external factors and more consistent in its output. PolyMoment can be used to calculate the standard deviation and minimise it

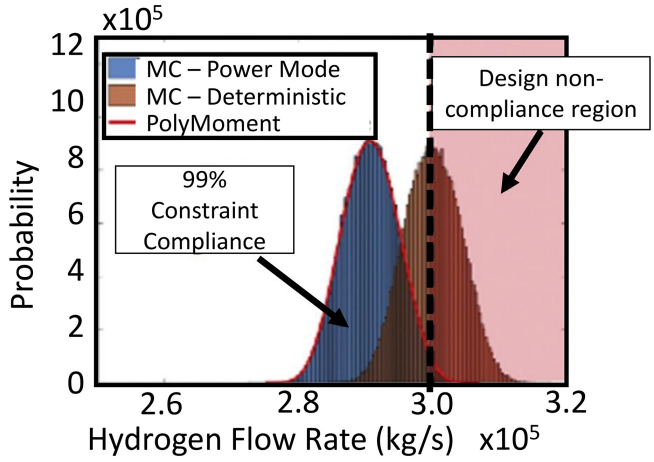

Figure 6.12. A comparison between the probability distribution obtained from the PolyMoment framework and those obtained using Monte Carlo simulations for the optimal parameter values that lead to the maximum output power. Reprinted from [28], Copyright 2018, with permission from Elsevier.

as an additional objective for a robust fuel cell design. Mathematically, the minimisation of these additional parameters can be added into the optimisation algorithm as follows:

$$\begin{aligned} &\text{minimize: } w_1\frac{\mu_{\mathrm{G}}}{\mu_{\mathrm{G}^0}} + w_2\frac{\sigma_{\mathrm{G}}}{\sigma_{\mathrm{G}^0}} + w_3\frac{\sigma_{W_{\mathrm{H}_2}}}{\sigma_{W^0_{\mathrm{H}_2}}}, \\ &\text{subject to: } W_{\mathrm{H}_2}(\mathbf{d}, \mathbf{X}) \leqslant 3\mathrm{e}^{-5} \text{ kg}, \\ &\quad \text{where: } \mathbf{d}^{\mathrm{L}} \leqslant \mathbf{d} \leqslant \mathbf{d}^{\mathrm{U}} \text{ and } \mathbf{d} = E[\mathbf{X}], \end{aligned} \tag{6.7}$$

where G^0 and $W^0_{\mathrm{H}_2}$ denote the initial values of the output power and hydrogen flow rate, respectively, and $\{w_1, w_2, w_3\}$ are weights assigned by the design engineer based on design priorities such that $w_1 + w_2 + w_3 = 1$. The standard deviations of both $G(\cdot)$ and $W_{\mathrm{H}_2}(\cdot)$ can be symbolically obtained from PolyMoment in figure 6.10.

The impacts of setting different priorities in the optimisation problem (6.7) were studied using three sets of weights $\{w_1, w_2, w_3\}$. Table 6.3 shows the values of three parameters of interest for all three scenarios obtained through MC simulation. The results show that the three scenarios lead to different fuel cell designs. The designer can choose the weights in problem (6.7) to balance the trade-off between maximising the mean power, the robustness of power, and the hydrogen flow rate. A trade-off and cost–benefit analysis is needed for the final optimal operating parameters. PolyMoment is a preferable option for uncertainty evaluation, as it is accurate, computationally efficient, and straightforward to use for design optimisation regardless of the problem's nonlinearity and dimensionality. Incorporating system uncertainties is crucial for a dependable and high-quality PEM fuel cell design, making it a valuable tool for design engineers.

Table 6.3. The differences in the mean and the standard deviation of a fuel cell's output power and the standard deviation of hydrogen flow rate for different weights in the optimisation problem shown in (6.7). The results were obtained using MC simulation.

Weights $\{w_1, w_2, w_3\}$	Mean output power, μ_G (W)	Standard deviation of the output power, σ_G (kg s^{-1})	Standard deviation of the hydrogen flow rate, $\sigma_{\dot{W}_{H_2}}$ (kg s^{-1})
{1,0,0}	1329.56	12.32	4.11e−7
$\left\{\frac{1}{3}, \frac{1}{3}, \frac{1}{3}\right\}$	1121.32	9.93	3.51e−7
$\left\{\frac{5}{9}, \frac{2}{9}, \frac{2}{9}\right\}$	1328.28	12.20	4.10e−7

6.5 Magnetic sensor module design

The design of magnetic sensors often involves the use of computer simulations, such as the FE modeling, followed by a design optimisation process to determine the optimal parameters that meet system constraints. However, this approach can be computationally expensive for high-dimensional systems and does not account for variations in manufacture that can lead to the production of noncompliant products. To address these shortcomings, this case study presents the use of a combined approach that uses the *parametric model order reduction* (PMOR) method and the reliability-based design optimisation method within the PolyMoment framework.

Specifically, it focuses on the design of a magnetic sensor for a linear motor mover position detector and uses a three-dimensional (3D) model. A new approach is proposed, incorporating *proper orthogonal decomposition* with *dynamic mode decomposition* (POD-DMD) [40, 41], multiparameter moment matching, and a response surface moment-based RBDO method that uses the PolyMoment framework to achieve an accurate and efficient analysis. This method reduces the risk of noncompliance caused by manufacturing uncertainties and provides a faster computational process. The design obtained from the presented method is compared to that obtained from a deterministic optimisation method to demonstrate its effectiveness.

Figure 6.13(a) displays a 3D view of the magnetic sensor and its placement on the stator of the linear motor in the *xyz* plane. The magnetic sensor module includes a Nd–Fe–B *permanent magnet* (PM) and three iron cores, labelled I, II, and III. A Hall integrated circuit is positioned between cores I and II. The PM is magnetised in the negative Y direction and the desired magnetic flux density B_X is measured at the midpoint of the airgap g_2 in the X direction.

The sensor operates by detecting changes in flux density caused by changes in reluctance. Due to the alternating tooth–slot structure of the linear motor stator, the flux density distribution at the midpoint of g_2 is sinusoidal for a two-pole pitch displacement. For the Hall integrated circuit to output a minimum of 1 V peak to peak, the sensor's *peak flux density* (PFD) must be at least 0.1 T. The *total harmonic distortion* (THD) should be less than 1%. To meet these requirements, the sensor must undergo a thorough parametric study and optimisation.

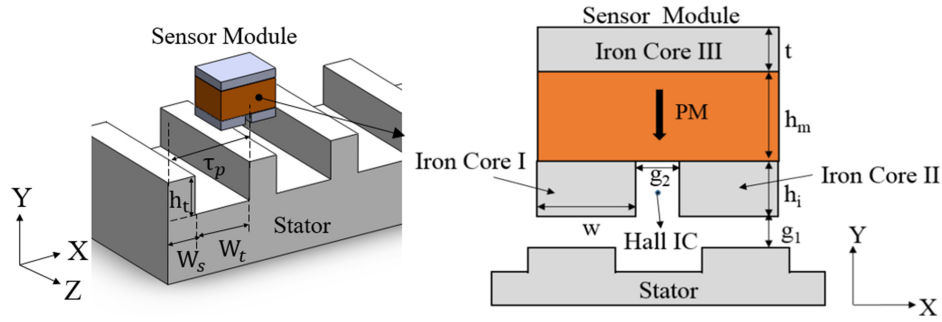

Figure 6.13. A linear position sensor module located on a stator. (a) The arrangement of the sensor module arrangement on the stator and (b) the parameters of the sensor module. PM denotes permanent magnet [42].

6.5.1 Problem formulation

Figure 6.14 shows the PMOR-RBDO framework, which starts with a POD-DMD-based PMOR method to achieve a computationally efficient result and then uses an RBDO technique to find the optimal sensor design that takes account of manufacturing uncertainties. To find the global optimum, this study uses the *genetic algorithm* (GA) as a heuristic method instead of gradient-based optimisers.

Equation (6.8) represents the mathematical model of the magnetic sensor module shown in figure 6.13, which is described as a nonlinear magnetostatic problem with no external electric source. In this equation, $\boldsymbol{M}$ and $\boldsymbol{K}$ are square matrices of size $n \times n$, $\boldsymbol{Y}(t)$ is the state vector, $\boldsymbol{F}(t)$ is the source vector, and $\boldsymbol{N}(t)$ is the nonlinearity associated with the system. The equation shows how the magnetic field $\boldsymbol{MY}(t)$ in the module is affected by the derivative of $\boldsymbol{Y}(t)$, the source vector $\boldsymbol{F}(t)$, and the nonlinearity $\boldsymbol{N}(t)$.

$$\boldsymbol{MY}(t) + \boldsymbol{K}\frac{d\boldsymbol{Y}(t)}{dt} = \boldsymbol{F}(t) + \boldsymbol{N}(\boldsymbol{Y}(t)) \tag{6.8}$$

To make this high-dimensional system more manageable, equation (6.6.1) is transformed into equation (6.6.2) using a combination of the singular value decomposition (SVD)-based POD method and the DMD [40, 43].

$$\boldsymbol{M}_r\boldsymbol{Y}_r(t) + \boldsymbol{K}_r\frac{d\boldsymbol{Y}_r(t)}{dt} = \Phi^*\boldsymbol{F}(t) + \Phi^*\Phi^{\mathrm{DMD}}\mathrm{diag}(e^{w^{\mathrm{DMD}}t})p, \tag{6.9}$$

where $p = (\Phi^{\mathrm{DMD}})^{\dagger}F_1$, $\boldsymbol{M}_r = \Phi^* M \Phi$, and $\boldsymbol{K}_r = \Phi^* K \Phi$. Φ^{DMD} are the DMD bases for rank k, p is the initial condition, and w_i are the eigenvalues. To include the effects of parameters on the system, multiparameter moment matching with the Taylor series is used to parameterise the equation. The magnetic sensor design is optimised using two different scenarios:

1. *Deterministic optimisation*: in this scenario, only the PMOR model is used, which does not account for the uncertainties in the design parameters due to manufacture. This method aims to optimise the peak flux density and total harmonic distortion without considering their tolerance effects.

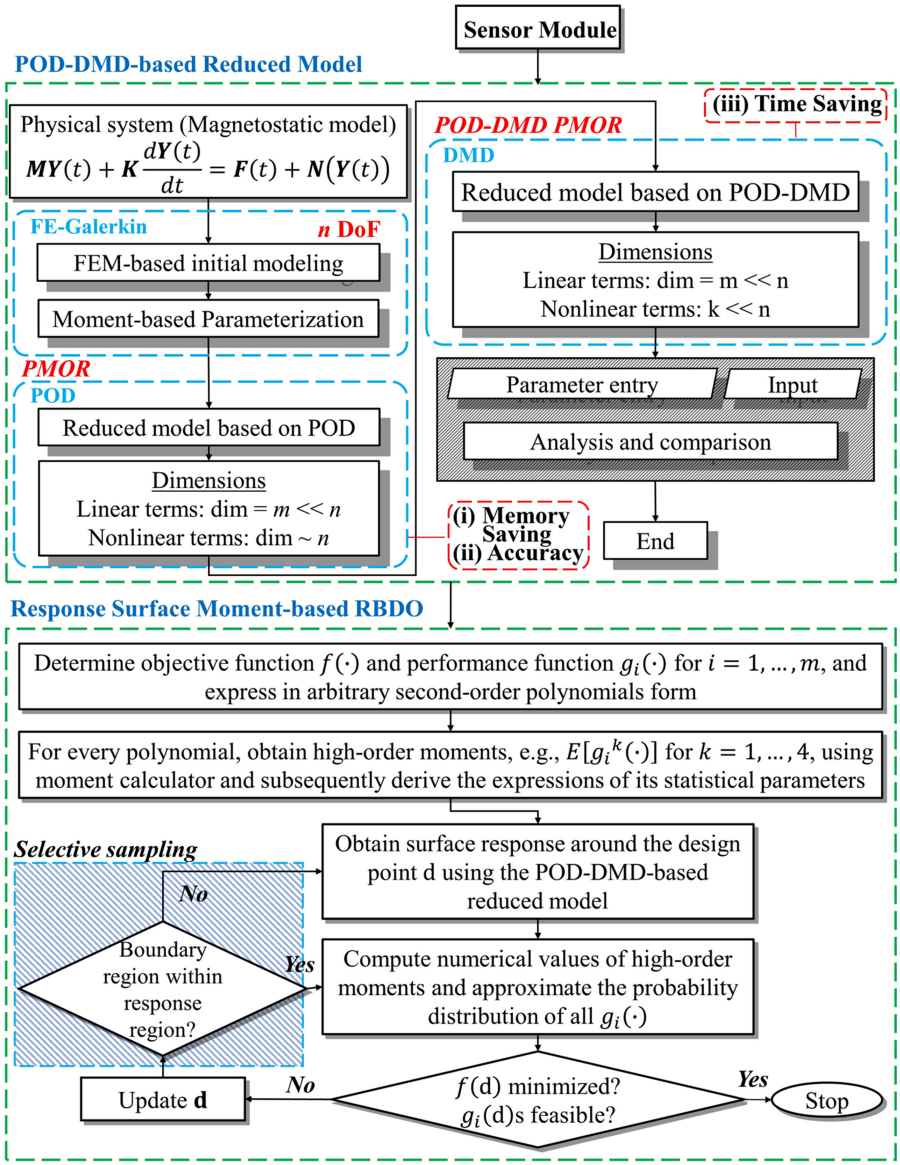

Figure 6.14. The flowchart of the PMOR-RBDO Framework. The RBDO portion of the flowchart, shown in the left half, incorporates the PolyMoment framework [42].

2. *Response surface moment-based RBDO*: in this scenario, the tolerance effects of the design parameters are considered during the optimisation, with a near-negligible failure probability of 0.01%. The optimisation takes account of the uncertainties caused by machines with tolerances of ±0.05 and ±0.1 mm. The actual constraint noncompliance is then calculated using the Monte Carlo method with 10^6 samples.

Table 6.4. Optimal design of the magnetic sensor and constraint compliance for deterministic optimisation and RBDO. FEV denotes function evaluation counts.

		Optimal design		Failure probability			
Optimisation method	Tolerance (mm)	PFD (T)	THD (%)	PFD (%)	THD (%)	Required FEV by GA	PMOR model calls
Deterministic (Scenario 1)	±0.05	0.13	0.24	0.63	0.00	2200	2200
	±0.1	0.13	0.24	10.97	0.00	2200	2200
RBDO (Scenario 2)	±0.05	0.16	0.24	0.00	0.00	58 600	7020
	±0.1	0.20	0.24	0.00	0.00	58 600	6560

6.5.2 The results of the PolyMoment-based RBDO method

The results are summarised in table 6.4, which shows that the deterministic design meets the set constraints but has a higher probability of failing to meet the required PFD constraint than the desired 0.01% because it does not consider the effects of manufacturing tolerance. Figure 6.15 shows that up to 11% of the probability distribution of the PFD could fail to meet the desired constraints for higher manufacturing uncertainties. On the other hand, RBDO avoids this problem and does not compromise the THD, as shown in table 6.4. The results also show that using the PMOR model and the proposed PolyMoment-based RBDO method improves the computational speed significantly compared to using the full FE model. The proposed method provides a significant improvement in terms of design noncompliance cost, computational speed, and accuracy, making it valuable for the production-ready design of magnetic sensors.

6.6 A multistorey three-dimensional steel structure: reliability analysis and optimisation

This section describes a case study in the field of structural design optimisation that focuses on a complex and challenging engineering problem. The study uses the PolyMoment-based RBDO method to evaluate uncertainty and ensure safety, by combining high-order moment-based uncertainty analysis with efficient response surface modelling. This method outperforms existing methods in terms of accuracy and computational efficiency, making it a significant case study in the field.

Figure 6.16 illustrates the finite element model of a five-story steel-framed modular building consisting of six identical corner-supported modules on each floor. The modules are 7.2 m long, 3.2 m wide, and 3.0 m high, with parallel-flange sections for beams and square hollow sections for columns. The floors are made of 100 mm thick concrete slabs, and all inter-module connections are assumed to be ideally pinned.

Uncertainties in steel-framed modular buildings often stem from the use of standardised prefabricated steel modules. When multiple modules are put together

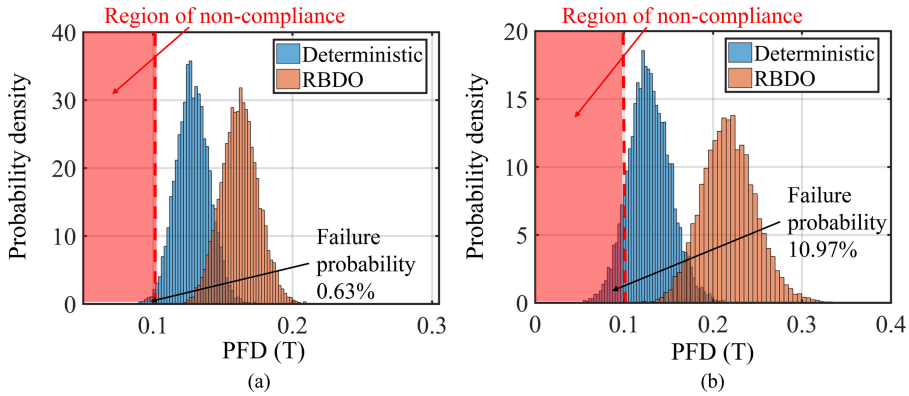

Figure 6.15. Probability distributions of the peak flux densities (PFDs) obtained using the MC method for deterministic and RBDO designs with manufacturing tolerances of (a) ±0.05 mm and (b) ±0.1 mm.

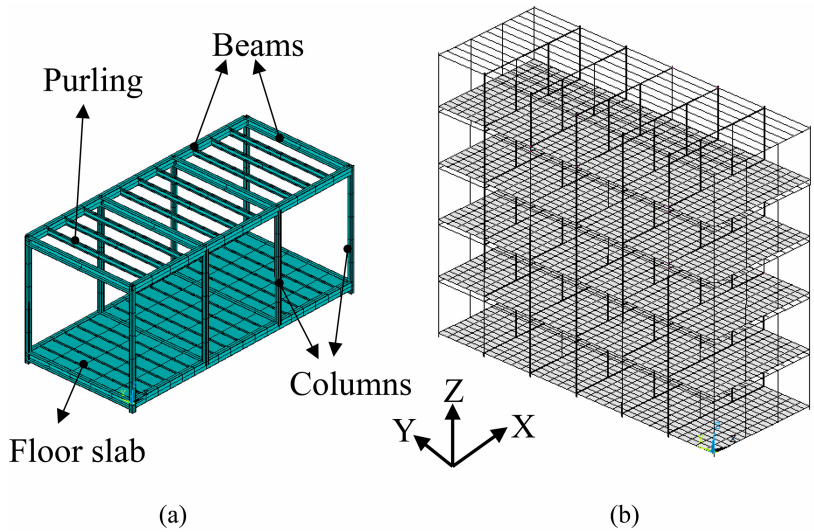

Figure 6.16. A three-dimensional multistorey structure in which (a) represents the single volumetric module and (b) represents the full structural model. Reprinted from [44], Copyright 2020, with permission from Elsevier.

to form a complex frame, it is crucial to consider the overall structural reliability. This is where the computational efficiency and accuracy of the PolyMoment method can be highly beneficial for engineers. The successful application of this method to a complex three-dimensional multistorey steel structure highlights its importance in understanding the implications of analytical uncertainty evaluation in engineering design.

6.6.1 Problem formulation

The FE model for the structure shown in figure 6.16 was obtained using the method outlined in [44]. The model represents a multistorey steel-framed structure that is

subjected to a combination of loads, including self-weight and superimposed dead load, live load, and wind load. The dead load calculation was performed using the ANSYS gravity field [45]. The wind load was determined based on the wind speed for Cyclonic Region C as per the Standards Association of Australia's AS1170.2 [46], and the design wind direction was assumed to be parallel to the global X-direction.

Three performance functions were selected, including G_1, which is the inter-storey drift under SLS loading (AS1170.0 [3]), G_2, which is the ULS performance of columns subjected to combined axial N_x^* and flexural actions M_y^* and M_z^* (AS4100 [47]), and G_3, which is the ULS performance of beams (AS4100 [47]). The structure was considered to have failed if any one of the performance functions was not met. The target reliability index was set at $\beta = 3$ for G_1 and $\beta = 3.8$ for G_2 and G_3, as per ISO 13822 [48].

In the optimisation process, variables such as M_{cx} and M_{cy} represent the member moment capacities in the principal and minor axes, respectively. N_{cx} is the column capacity, Z_{be} and Z_{ce} are the section modules for beams and columns, respectively, A_b and A_c are the cross-sectional areas of beams and columns, and details such as the material and geometric properties can be found in table 6.5. The probabilistic models for load variables in this table were determined based on the Australian Building Codes Board Handbook [49] and the material models based on the Joint Committee on Structural Safety code [50].

The starting point for the optimisation was set at $\{w_c, t_c, w_{fb}, d_{bb}, t_{fb}, t_{wb}\} = \{100, 9.0, 133, 202, 7.0, 5.0\}$ mm. The optimisation of the structure was carried out by minimising the total volume of the columns and beams and reducing the structural self-weight, as described in detail below:

$$
\begin{aligned}
\text{find:} \quad & w_c,\ t_c,\ w_{fb},\ d_{bb},\ t_{fb} \text{ and } t_{wb} \\
\text{minimise:} \quad & f = \sum L_c A_c + \sum L_b A_b \\
\text{subject to:} \quad & G_1 = \Delta - \frac{H}{500} \leqslant 0 \\
& G_2 = \left(\frac{M_y^*}{M_{cy}}\right)^{1.4} + \left(\frac{M_z^*}{M_{cz}}\right)^{1.4} \leqslant 1, \\
& \text{where } M_{ci} = M_{cs}\left(1 - \frac{N_x^*}{N_{cx}}\right) \text{ for } i \\
& \quad = x,\ y,\ N_{cx} = \alpha_c A_c f_y \text{ and} \\
& \quad M_{cs} = Z_{ce} f_y \\
& G_3 = \alpha_m \alpha_s M_{bs}, \quad \text{where } M_{bs} = Z_{be} f_y, \\
& \text{where: } \alpha_m = 1.0 H = 3 \text{ m} \sum L_c = 720 \sum L_b = 1248.
\end{aligned}
\tag{6.10}
$$

Table 6.5. Properties of the random variables for the three-dimensional multistorey structure problem; CoV denotes the coefficient of variation.

	Description	Distribution	Median		CoV
			SLS	ULS	
$SIDL$	Superimposed dead load (Pa)	Lognormal	1000		0.10
LL	Live load (Pa)	Lognormal	1500		0.43
w_c	Width of column (Pa)	Normal	Not applicable		0.0205
t_c	Wall thickness of column (Pa)	Normal	Not applicable		0.0362
w_{fb}	Flange width of beam (Pa)	Normal	Not applicable		0.0132
d_{bb}	Depth of beam (Pa)	Normal	Not applicable		0.0364
t_{fb}	Flange thickness of beam (Pa)	Normal	Not applicable		0.0182
t_{wb}	Web thickness of beam (Pa)	Normal	Not applicable		0.0151
E_s	Elastic modulus of steel (Pa)	Lognormal	206×10^9		0.03
E_c	Elastic modulus of concrete (Pa)	Lognormal	21.8×10^9		0.15
p_W	Windward wind pressure (Pa)	Lognormal	169.5040	432.0960	0.16
p_L	Leeward wind pressure (Pa)	Lognormal	56.4987	144.0309	0.16
p_R	Roof wind pressure (Pa)	Lognormal	169.4961	432.0927	0.16
Rou_S	Density of steel (kg m^{-3})	Lognormal	7700		0.01
Rou_C	Density of concrete (kg m^{-3})	Lognormal	2400		0.04
f_y	Yield stress of steel (Pa)	Lognormal	350×10^6		0.05

6.6.2 The resultant design and benchmarking

Table 6.6 presents the results of the RBDO problem for the complex steel structure shown in figure 6.16; in this table, reliability analysis based on PMA from section 3.2 is utilised to compare the outcomes of the PolyMoment method, which was applied with up to $N_m = 4$ and $N_m = 8$ moments. The table reports the reliability indexes of the final RBDO designs, which were obtained from the ANSYS model of the structure. The reliability indexes were calculated using the Monte Carlo method. Only the final reliability index of performance function G_1 is shown in table 6.6, as the reliability indexes of both G_2 and G_3 are infinite. This implies that G_1 is the only constraint that plays a role in determining the final design.

The results reveal that the PolyMoment-based method requires significantly fewer function evaluations (540 evaluations) compared to the PMA method (6022 evaluations), leading to an approximately elevenfold increase in computational efficiency. The design obtained using the PolyMoment method meets the target reliability index of $\beta = 3$ as described in (6.10), while the design obtained using the MPP-based RBDO method does not meet this target, potentially resulting in an underdesigned structure.

In addition, the results in table 6.6 show that the use of higher-order moments improves the accuracy of the reliability analysis and results in a more optimum final design with a lower total cross-sectional area, without sacrificing the number of

Table 6.6. RBDO results for the three-dimensional multistorey structure problem. The reliability indexes β of G_2 and G_3 are infinite. The PMA was employed using a recent MPP-based algorithm provided in [51] for reliability analysis.

Method	Final design							FEV counts	β of G_1
	w_c	t_c	w_{fb}	d_{bb}	t_{fb}	t_{wb}	C		
Deterministic	0.0947	0.0050	0.0750	0.2300	0.0120	0.0060	5.0801	120	
PMA	0.0988	0.0050	0.0750	0.2300	0.0120	0.0060	5.1828	6022	2.8043
PolyMoment ($N_m = 4$)	0.0976	0.0050	0.0750	0.2300	0.0120	0.0060	5.2000	540	3.0274
PolyMoment ($N_m = 8$)	0.0968	0.0050	0.0750	0.2300	0.0120	0.0060	5.1108	540	3.0107

function evaluations. This efficiency and accuracy improvement is due to the absence of MPP iterations in finding the reliability constraints and the selective sampling paradigm in finding the local response surface models.

It is important to note that while the localised response surface with selective sampling mechanism could be used for MPP-based methods, the added assumptions on top of the MPP transformation and search strategies may negatively affect its reliability constraint evaluation accuracy. As such, the PolyMoment-based probabilistic optimisation methodology is a more desirable choice for complex problems, especially for safety-critical structural designs that are required to meet building standards and their reliability constraints, such as wind and earthquakes.

6.7 Summary

This chapter presented a unified moment-based probabilistic optimisation framework called the PolyMoment-based approach, which is generic and can be adapted to RDO, RBDO, and RBRDO optimisation paradigms. The methodology was explained in detail and its use was demonstrated through five real-world applications: lithium-ion batteries, vehicle side-impact crashworthiness, a magnetic sensor module, and a multistorey steel structure.

References

[1] Missoum S, Ramu P and Haftka R T 2007 A convex hull approach for the reliability-based design optimization of nonlinear transient dynamic problems *Comput. Meth. Appl. Mech. Eng.* **196** 2895–906

[2] Youn B D and Choi K K 2004 A new response surface methodology for reliability-based design optimization *Comput. Struct.* **82** 241–56

[3] 2002 *Structural design action—part 0: general principles* AS/NZS 1170.0:2002 Standards New Zealand https://www.standards.govt.nz/shop/asnzs-1170-02002

[4] Mansour R and Olsson M 2016 Response surface single loop reliability-based design optimization with higher-order reliability assessment *Struct. Multidiscip. Optim.* **54** 63–79

[5] Chen Z, Qiu H, Gao L, Li X and Li P 2014 A local adaptive sampling method for reliability-based design optimization using Kriging model *Struct. Multidiscip. Optim.* **49** 401–16
[6] Shang Y-W and Qiu Y-H 2006 A note on the extended Rosenbrock function *Evol. Comput.* **14** 119–26
[7] Rajan A, Vijayaraghavan V, Ooi M P-L, Garg A and Kuang Y C 2018 A simulation-based probabilistic framework for lithium-ion battery modelling *Measurement* **115** 87–94
[8] Abaqus version 6.10. *Abaqus User Subroutines Reference Manual*, Providence, RI Dassault Systèmes Simulia Corp., 2010
[9] Sahraei E, Kahn M, Meier J and Wierzbicki T 2015 Modelling of cracks developed in lithium-ion cells under mechanical loading *RSC Adv.* **5** 80369–80
[10] Dufo-López R, Lujano-Rojas J M and Bernal-Agustín J L 2014 Comparison of different lead–acid battery lifetime prediction models for use in simulation of stand-alone photovoltaic systems *Appl. Energy* **115** 242–53
[11] Yarime M, Shiroyama H and Kuroki Y 2008 The strategies of the Japanese auto industry in developing hybrid and fuel cell vehicles *Making Choices about Hydrogen: Transport Issues for Developing Countries* (Tokyo: UNU Press) pp 187–212 https://www.idrc.ca/en/book/making-choices-about-hydrogen-transport-issues-developing-countries International Development Research Centre (IDRC)
[12] Young K, Wang C, Wang L Y and Strunz K 2013 Electric vehicle battery technologies *Electric Vehicle Integration into Modern Power Networks* (New York: Springer) pp 15–56
[13] Iman R 2008 Latin Hypercube Sampling *Encyclopedia of Statistical Sciences* (Hoboken, NJ: Wiley)
[14] Draper N 1995 *Response Surface Methodology: Process and Product Optimization Using Designed Experiments: RH Myers and DC Montgomery* vol 59 (New York: Wiley) p 714
[15] Nocedal J and Wright S J 2006 Quadratic programming *Numerical Optimization* (New York: Springer) pp 448–92
[16] Deb K, Pratap A, Agarwal S and Meyarivan T 2002 A fast and elitist multiobjective genetic algorithm: NSGA-II *IEEE Trans. Evol. Comput.* **6** 182–97
[17] Tian Q, Zhao D, Li Z and Zhu Q 2017 Robust and stepwise optimization design for CO_2 pipeline transportation *Int. J. Greenhouse Gas Control* **58** 10–8
[18] Zhao D, Tian Q, Li Z and Zhu Q 2016 A new stepwise and piecewise optimization approach for CO_2 pipeline *Int. J. Greenhouse Gas Control* **49** 192–200
[19] Youn B D, Choi K, Yang R-J and Gu L 2004 Reliability-based design optimization for crashworthiness of vehicle side impact *Struct. Multidiscip. Optim.* **26** 272–83
[20] W. G. European Enhanced Vehicle-Safety Committee *Side Impact* https://eevc.net/EEVC/EN/Past/WG09/WG09.html (accessed January 2023)
[21] Rajan A, Ooi M, Kuang Y C and Demidenko S 2017 Reliability-based design optimisation of technical systems: analytical response surface moments method *J. Eng.* **2017** 36–46
[22] Valdebenito M A and Schuller G I 2010 A survey on approaches for reliability-based optimization *Struct. Multidiscip. Optim.* **42** 645–63
[23] Åhman M 2001 Primary energy efficiency of alternative powertrains in vehicles *Energy* **26** 973–89
[24] Schäfer A, Heywood J B and Weiss M A 2006 Future fuel cell and internal combustion engine automobile technologies: a 25-year life cycle and fleet impact assessment *Energy* **31** 2064–87

[25] Corbo P, Migliardini F and Veneri O 2007 Performance investigation of 2.4 kW PEM fuel cell stack in vehicles *Int. J. Hydrog. Energy* **32** 4340–9
[26] Srinivasan S, Velev O A, Parthasarathy A, Manko D J and Appleby A J 1991 High energy efficiency and high power density proton exchange membrane fuel cells—electrode kinetics and mass transport *J. Power Sources* **36** 299–320
[27] Verbrugge M W and Hill R F 1990 Ion and solvent transport in ion-exchange membranes: II. A radiotracer study of the sulfuric-acid, nation-117 system *J. Electrochem. Soc.* **137** 893
[28] Rajan A, Garg A, Vijayaraghavan V, Kuang Y C and Ooi M P-L 2018 Parameter optimization of polymer electrolyte membrane fuel cell using moment-based uncertainty evaluation technique *J. Energy Storage* **15** 8–16
[29] Xuan D, Li Z, Kim J and Kim Y 2009 Optimal operating points of PEM fuel cell model with RSM *J. Mech. Sci. Technol.* **23** 717–28
[30] Park C, Oh K, Kim D and Kim H 2004 Development of fuel cell hybrid electric vehicle performance simulator *Int. J. Automot. Technol.* **5** 287–95 http://www.ijat.net/journal/view.php?number=194
[31] Al-Baghdadi M A S and Al-Janabi H A S 2007 Parametric and optimization study of a PEM fuel cell performance using three-dimensional computational fluid dynamics model *Renew. Energy* **32** 1077–101
[32] Sikha G and Popov B N 2004 Performance optimization of a battery–capacitor hybrid system *J. Power Sources* **134** 130–8
[33] Kim M-J and Peng H 2007 Power management and design optimization of fuel cell/battery hybrid vehicles *J. Power Sources* **165** 819–32
[34] San F G B, Isik-Gulsac I and Okur O 2013 Analysis of the polymer composite bipolar plate properties on the performance of PEMFC (polymer electrolyte membrane fuel cells) by RSM (response surface methodology) *Energy* **55** 1067–75
[35] Okur O, Alper E and Almansoori A 2014 Optimization of catalyst preparation conditions for direct sodium borohydride fuel cell using response surface methodology *Energy* **67** 97–105
[36] Kanani H, Shams M, Hasheminasab M and Bozorgnezhad A 2015 Model development and optimization of operating conditions to maximize PEMFC performance by response surface methodology *Energy Convers. Manage.* **93** 9–22
[37] Charoen K *et al* 2017 Application of response surface methodology to optimize direct alcohol fuel cell power density for greener energy production *J. Clean. Prod.* **142** 1309–20
[38] Garg A, Panda B N and Lam J S L 2016 Functional characterization of current characteristic of direct methanol fuel cell *Fuel* **183** 432–40
[39] Fesanghary M, Mahdavi M, Minary-Jolandan M and Alizadeh Y 2008 Hybridizing harmony search algorithm with sequential quadratic programming for engineering optimization problems *Comput. Meth. Appl. Mech. Eng.* **197** 3080–91
[40] Tu J H, Luchtenburg D M, Rowley C W, Brunton S L and Kutz J N 2013 Novel sampling strategies for dynamic mode decomposition *66th Annual Meeting of the APS Division of Fluid Dynamics* 58 (College Park, MD: American Physical Society) APS Division of Fluid Dynamics Meeting Abstracts, H35.001 http://meetings.aps.org/link/BAPS.2013.DFD.H35.1
[41] Chatterjee A 2000 An introduction to the proper orthogonal decomposition *Curr. Sci.* **78** 808–17 https://www.currentscience.ac.in/Volumes/78/07/0808.pdf

[42] Paul S, Rajan A, Chang J, Kuang Y C and Ooi M P-L 2018 Parametric design analysis of magnetic sensor based on model order reduction and reliability-based design optimization *IEEE Trans. Magn.* **54** 1–4

[43] Paul S and Chang J 2017 Design and parametric study of the magnetic sensor for position detection in linear motor based on nonlinear parametric model order reduction *Sensors* **17** 1543

[44] Rajan A, Luo F J, Kuang Y C, Bai Y and Ooi M P-L 2020 Reliability-based design optimisation of structural systems using high-order analytical moments *Struct. Saf.* **86** 101970

[45] Stolarski T, Nakasone Y and Yoshimoto S 2018 *Engineering Analysis with ANSYS Software* 2 (Oxford: Butterworth-Heinemann)

[46] 2011 *Structural design actions - Part 2: Wind actions* AS/NZS 1170.2:2011 Standards New Zealand https://www.standards.govt.nz/shop/asnzs-1170-22011/

[47] 2016 *Steel structures* AS 4100—1998 Standards Australia https://www.standards.org.au/standards-catalogue/sa-snz/building/bd-001/as—4100-1998

[48] ISO 13822:2010 2010 *Bases for design of structures—Assessment of existing structures* (International Organisation for Standardization)

[49] 2019 *Handbook: Structural Reliability Verification Method* 1.0 (Canberra: Australian Building Codes Board)

[50] 2001 Probabilistic model code part 2: load models https://www.jcss-lc.org/jcss-probabilistic-model-code/ Joint Committee on Structural Safety https://www.jcss-lc.org/jcss-probabilistic-model-code/

[51] Roudak M A, Shayanfar M A, Barkhordari M A and Karamloo M 2017 A robust approximation method for nonlinear cases of structural reliability analysis *Int. J. Mech. Sci.* **133** 11–20